Monthly Notices of the ROYAL ASTRONOMICAL SOCIETY

MNRAS **530,** 730–742 (2024) https://doi.org/10.1093/mnras/stae781
Advance Access publication 2024 March 18

Magnetospheric flows in X-ray pulsars – I. Instability at super-Eddington regime of accretion

A. A. Mushtukov [1★], A. Ingram [2], V. F. Suleimanov [3], N. DiLullo,[4] M. Middleton,[5] S. S. Tsygankov [6], M. van der Klis[7] and S. Portegies Zwart[8]

[1]*Astrophysics, Department of Physics, University of Oxford, Denys Wilkinson Building, Keble Road, Oxford OX1 3RH, UK*
[2]*School of Mathematics, Statistics and Physics, Newcastle University, Herschel Building, Newcastle upon Tyne, NE1 7RU, UK*
[3]*Institut für Astronomie und Astrophysik, Kepler Center for Astro and Particle Physics, Universität Tübingen, Sand 1, D-72076 Tübingen, Germany*
[4]*Thacher School, 5025 Thacher Road, Ojai, CA 93023-8304, USA*
[5]*Department of Physics and Astronomy, University of Southampton, Highfield, Southampton SO17 1BJ, UK*
[6]*Department of Physics and Astronomy, University of Turku, FI-20014 Turku, Finland*
[7]*Anton Pannekoek Institute, University of Amsterdam, Science Park 904, NL-1098 XH Amsterdam, the Netherlands*
[8]*Leiden Observatory, Leiden University, NL-2300 RA Leiden, the Netherlands*

Accepted 2024 March 11. Received 2024 February 18; in original form 2023 October 21

ABSTRACT

Within the magnetospheric radius, the geometry of accretion flow in X-ray pulsars is shaped by a strong magnetic field of a neutron star. Starting at the magnetospheric radius, accretion flow follows field lines and reaches the stellar surface in small regions located close to the magnetic poles of a star. At low mass accretion rates, the dynamics of the flow is determined by gravitational attraction and rotation of the magnetosphere due to the centrifugal force. At the luminosity range close to the Eddington limit and above it, the flow is additionally affected by the radiative force. We construct a model simulating accretion flow dynamics over the magnetosphere, assuming that the flow strictly follows field lines and is affected by gravity, radiative, and centrifugal forces only. The magnetic field of a neutron star is taken to be dominated by the dipole component of arbitrary inclination with respect to the accretion disc plane. We show that accretion flow becomes unstable at high mass accretion rates and tends to fluctuate quasi-periodically with a typical period comparable to the free-fall time from the inner disc radius. The inclination of a magnetic dipole with respect to the disc plane and strong anisotropy of X-ray radiation stabilize the mass accretion rate at the poles of a star, but the surface density of material covering the magnetosphere fluctuates even in this case.

Key words: accretion, accretion discs – magnetic fields – stars: neutron – stars: oscillations – X-rays: binaries.

1 INTRODUCTION

X-ray pulsars (XRPs) are accreting strongly magnetized neutron stars (NSs) in compact binary systems (see Mushtukov & Tsygankov 2022 for recent review). Magnetic field at the NS surface in XRPs confirmed by detection of the cyclotron lines (Staubert et al. 2019) is known to be of the order of 10^{12} G or even stronger. Large-scale magnetic field is expected to be dominated by the dipole component (that can be distorted by the accretion process; see Lai 2014 for review), but in some specific cases there was reported possibility of the field heavily contributed by non-dipole components (see e.g. Israel et al. 2017a; Tsygankov et al. 2017; Mönkkönen et al. 2022). Observed luminosity of XRPs covers more than seven orders of magnitude from 10^{32} up to 10^{41} erg s^{-1}. The lower edge of accretion luminosity range is partly related to the onset of the 'propeller' state of accretion when the centrifugal barrier due to the rotating NS magnetosphere prevents accretion on to the stellar surface (Illarionov & Sunyaev 1975; Raguzova & Lipunov 1998; Ustyugova et al. 2006). The brightest XRPs belong to the class of recently discovered pulsating ultraluminous X-ray sources (ULXs; see Bachetti et al. 2014; Fürst et al. 2016; Israel et al. 2017a, b; Carpano et al. 2018; Fabrika et al. 2021; King, Lasota & Middleton 2023 for review). The apparent luminosity of the brightest ULX pulsar – NGC5907 X-1 – exceeds 10^{41} erg s^{-1} (Israel et al. 2017a). The relation between the actual and apparent luminosities of bright XRPs is still debated by the community. Specific geometry of X-ray emission region in close proximity to an NS surface does not significantly affect the apparent luminosity of bright XRPs (see e.g. Markozov & Mushtukov 2024). However, there are arguments in favour of a large difference between actual and apparent luminosities due to the geometrical beaming at high mass accretion rates (King 2009; King, Lasota & Kluźniak 2017; King & Lasota 2020) expected because of possibly strong radiation-driven outflows launched from accretion discs (Shakura & Sunyaev 1973; Poutanen et al. 2007; King 2009; Jiang, Stone & Davis 2014). At the same time, it has been shown that strong beaming of X-ray radiation is inconsistent with large pulsed fraction observed in six ULX pulsars known up to date, which says in favour of relatively small difference between the actual and apparent luminosities (Mushtukov et al. 2021; Mushtukov & Portegies Zwart 2023).

Accretion flow in the systems hosting strongly magnetized NSs is truncated by magnetic field of an NS at the magnetospheric radius $R_{\rm m}$, which is determined by the NS magnetic field strength,

★ E-mail: alexander.mushtukov@physics.ox.ac.uk

mass accretion rate at $R_{\rm m}$, and geometry of the accretion flow (i.e. disc/wind accretion, disc thickness, and physical conditions in it; see Chashkina et al. 2019 for detailed discussion). At the magnetospheric radius, the flow penetrates into the magnetosphere due to the instabilities, including magnetic Rayleigh–Taylor (Arons & Lea 1976; Kulkarni & Romanova 2008) and Kelvin–Helmholtz instabilities (Burnard, Arons & Lea 1983). Development of the instabilities results in the formation of a boundary layer between the disc and magnetosphere of an NS (Lai 2014). In the boundary layer, the angular velocity of plasma experiences a transition from the Keplerian rate to the NS spin rate.

Within the magnetospheric radius, the flow follows magnetic field lines and finally reaches the surface of an NS within small regions (area $\sim 10^{10}$ cm^2; see section 4.3 in Mushtukov & Tsygankov 2022) located close to the magnetic poles of a star. Depending on the mass accretion rate and corresponding energy release, the flow is stopped due to the Coulomb collisions in the atmosphere of an NS (expected for $\dot{M} \lesssim 10^{17}$ g s^{-1}; see e.g. Zel'dovich & Shakura 1969; Nelson et al. 1995) or at the radiation pressure-dominated shock above NS surface (expected for the case of $\dot{M} \gtrsim 10^{17}$ g s^{-1}; see Basko & Sunyaev 1976; Wang & Frank 1981; Zhang, Blaes & Jiang 2022).

The dynamics of accretion flow in between the magnetospheric radius and NS surface is determined by the geometry of magnetic field lines, gravitational force, centrifugal force, and radiative force, which comes into play at sufficiently high mass accretion rates. Stable accretion flow covering the magnetosphere of an NS is expected to be optically thick at high mass accretion rates ($\dot{M} \gtrsim$ few $\times 10^{18}$ g s^{-1}) typical for ULX pulsars and bright Be XRPs (Reig 2011) at the peaks of their outbursts (see e.g. Mushtukov et al. 2017, 2019a). The optically thick envelope might strongly affect the key observational properties of bright XRPs, including their energy spectra, X-ray polarization, pulse profiles, and timing properties of aperiodic variability.

This paper presents the first simulations of accretion flow dynamics between the inner disc radius and NS surface. We account for the geometry of accretion flow shaped by a magnetic field of an NS and the influence of gravitational, centrifugal, and radiative forces. The stellar magnetic field is assumed to be purely dipole with a given arbitrary inclination of the magnetic dipole with respect to the accretion disc plane.

2 MODEL SET-UP

2.1 Geometry of accretion flow

In this paper, we consider a particular case of accretion from the disc; i.e. the material starts its motion towards the poles of an NS from a specific region, where the disc is interrupted by the B-field. We assume that the rotational axis of an NS is orthogonal to the accretion disc plane, which is likely a case in strongly magnetized accreting NSs. The disc in XRPs is interrupted at the magnetospheric radius $R_{\rm m}$, which is dependent on the mass accretion rate, NS magnetic field strength, and structure. In the case of the field dominated by the dipole component, $R_{\rm m}$ can be estimated as

$$R_{\rm m} \approx 1.8 \times 10^8 \, \Lambda \, B_{12}^{4/7} \dot{M}_{17}^{-2/7} m^{-1/7} R_6^{12/7} \ {\rm cm}, \tag{1}$$

where $\Lambda < 1$ is a factor depending on the accretion flow geometry (see e.g. chapter 6.3 in Frank, King & Raine 2002; Chashkina et al. 2019 for recent discussion related to the case of high mass accretion rates), B_{12} is the surface magnetic field strength in units of 10^{12} G, $\dot{M}_{17}$ is the mass accretion rate in units of 10^{17} g s^{-1}, m is the mass of an NS M in units of $\mathrm{M}_\odot$, and R_6 is the NS radius in units of 10^6 cm.

The effective temperature in accretion disc can be estimated as

$$\sigma_{\rm SB} T_{\rm eff}^4 = \frac{3}{8\pi} \frac{GM\dot{M}}{r^3} \left[1 - \beta \left(\frac{R_{\rm m}}{r} \right)^{1/2} \right], \tag{2}$$

where $\sigma_{\rm SB}$ is the Stefan–Boltzmann constant, and r is the distance from a central compact object, and $\beta \in [0; 1]$ is a coefficient determined by a distance where stress disappears ($\beta = 1$ in the case of stress disappearance at $R_{\rm m}$, while $\beta = 0$ corresponds to stress disappearance at $r \ll R_{\rm m}$). Combining equations (1) and (2), we can roughly estimate the effective temperature at the inner disc radius as

$$T_{\rm eff} \lesssim 0.03 \, B_{12}^{-3/7} \dot{M}_{17}^{13/28} \ {\rm keV}. \tag{3}$$

The temperature of plasma settling magnetic field lines at the inner disc radius is probably higher because equations (2) and (3) do not account for the interaction between the magnetosphere of an NS and accretion disc.

We assume that the accretion flow within the magnetospheric radius cannot move across magnetic field lines. In the spherical coordinates (r, θ, φ), the geometry of a dipole field line is given by

$$r = R_{\rm max} \cos^2 \lambda = R_{\rm max} \sin^2 \theta, \tag{4}$$

where $R_{\rm max}$ is a linear scale describing dipole magnetic field line, λ is the latitude, and $\theta = \pi/2 - \lambda$ is the corresponding co-latitude in the reference frame related to the B-field. The linear scale of a field line $R_{\rm max}$ in equation (4) is typically assumed to be equal to $R_{\rm m}$, but it is a case of magnetic dipole aligned with the disc only. In the case of inclined magnetic dipole,

$$R_{\rm max} = R_{\rm m} \sin^{-2} \theta_{\rm d}, \tag{5}$$

where

$$\theta_{\rm d} = {\rm atan}(\sin^{-1} \varphi \tan^{-1} \alpha) \tag{6}$$

is the co-latitude, where the disc plane crosses the dipole surface, and α is the magnetic obliquity, i.e. the angle between the rotational axis of the NS and the magnetic dipole axis (see Fig. 1). Assuming the inner disc radius independent of the azimuthal coordinate, we get $R_{\rm max}$ dependent on φ and magnetic obliquity α.

The area on the dipole surface S is related to the latitude λ and the azimuthal angle φ as

$${\rm d}S = R_{\rm max}^2 \cos^4 \lambda (1 + 3 \sin^2 \lambda)^{1/2} {\rm d}\lambda {\rm d}\varphi, \tag{7}$$

while the length along the field lines x is related to the latitude as

$${\rm d}x = R_{\rm max} \cos \lambda (1 + 3 \sin^2 \lambda)^{1/2} {\rm d}\lambda. \tag{8}$$

The angle between the position vector of the point at the dipole surface and the tangent line to the dipole magnetic field line (see Fig. 2) is

$$\chi = {\rm atan}[0.5 \tan^{-1} \lambda]. \tag{9}$$

Further in this paper, we present maps describing the distribution of different quantities (accelerations, surface density, etc.) over the dipole surface of an NS magnetosphere. The position of a point on the dipole surface ($R_{\rm max}$ is fixed) is uniquely given by two angles: λ (or θ) and φ. To represent magnetospheric maps, we apply Aitoff transformation to the coordinates λ and φ, as is standardly done to represent maps of spherical surfaces:

$$x_{\rm pr} = \frac{2\varrho \sin(\lambda/2) \cos \varphi}{\sin \varrho}, \qquad y_{\rm pr} = \frac{\varrho \sin \varphi}{\sin \varrho}, \tag{10}$$

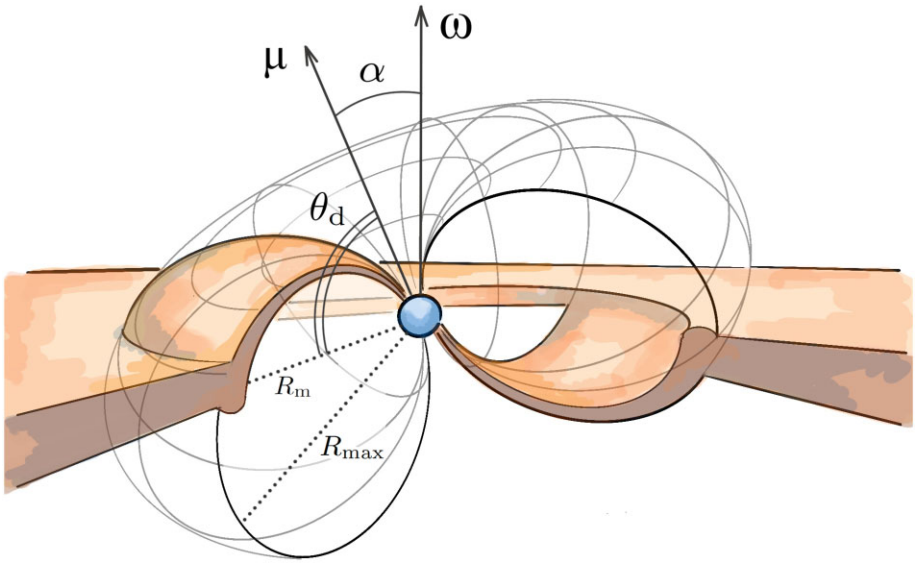

Figure 1. Schematic illustration of accretion geometry on to strongly magnetized NS. Magnetic field is considered to be dominated by the dipole component, while the rotation axis is assumed to be orthogonal to the accretion disc plane.

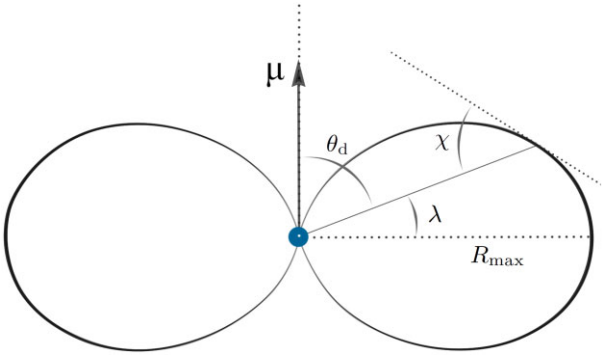

Figure 2. The schematic geometry of dipole magnetic field line, where $R_{\rm max}$ is the linear scale describing magnetic field line, λ ($\theta_{\rm d}$) is the latitude (co-latitude) of a point, and χ is the angle between the position point and the tangent line to the field line (9).

where

$$\varrho = \arccos\left(\cos\frac{\lambda}{2}\cos\varphi\right).$$

2.2 Dynamics of accretion flow

We consider the accretion flow moving under the influence of three forces: the gravitational, the radiative, and the centrifugal force. We assume that the flow covering the magnetosphere of an NS is supersonic and do not account for the influence of internal gas pressure gradients.

The gravitational force is directed towards the compact object, and the corresponding acceleration along the dipole field line is given by

$$\left|a_{\rm grav,||}\right| = \cos\chi\,\frac{GM}{r^2} \simeq 1.328\times10^{10}\,m r_8^{-2}\cos\chi\ {\rm cm\,s^{-2}}. \quad (11)$$

The gravitational acceleration along the field lines turns to zero at the equator. At $\lambda > 0$ ($\lambda < 0$), the acceleration $a_{\rm grav,||}$ is positive (negative). Its absolute value of the acceleration increases towards to the central object.

The centrifugal force is directed perpendicularly to the rotational axis of an NS and dependent on the NS spin period and specific point on the magnetospheric surface. In the particular case of magnetic dipole aligned with the rotational axis, the corresponding centrifugal acceleration along the field lines is given by

$$a_{\rm cen,||}(\alpha=0) = \omega^2 R_{\rm m}\cos^3\lambda\cos(\chi-\lambda), \quad (12)$$

where ω is the angular velocity of an NS. In a general case of inclined magnetic dipole, equation (12) has to be calculated as

$$a_{\rm cen,||} = -\boldsymbol{n}_B\cdot[\boldsymbol{\omega}\times(\boldsymbol{\omega}\times\boldsymbol{r})], \quad (13)$$

where $\boldsymbol{n}_B$ is the unit vector directed along the magnetic field line, '$\cdot$' and '$\times$' denote the scalar and the vector productions, respectively. In the particular case of the orthogonal rotator (i.e. $\alpha = \pi/2$), equation (13) is reduced to

$$a_{\rm cen,||}(\alpha=\pi/2) = \omega^2 R_{\rm max}\cos^2\lambda\cos\chi. \quad (14)$$

The total acceleration along the field lines due to the gravitational and centrifugal forces is dependent on the inclination of the magnetic dipole with respect to the rotation axis and NS spin period. In general, the acceleration is dependent both on the latitude and the azimuth angle (see Fig. 3). Sufficiently small spin periods result in the appearance of regions with acceleration directed towards the disc plane, i.e. total acceleration due to the gravitational and centrifugal forces tends to prevent accretion flow from its motion towards the poles of an NS. It is the centrifugal barrier, which can lead to the propeller regime of accretion in XRPs (Illarionov & Sunyaev 1975; Ustyugova et al. 2006). It is expected that the accretion flow is able to penetrate through the centrifugal barrier in the case of the sufficiently high initial velocity of the flow or in the case of a sufficient geometrical thickness of the disc (some aspects of the influence of accretion disc geometrical thickness on the propeller regime were discussed by Çıkıntoğlu & Ekşi 2023). In the case of a magnetic dipole inclined to the rotation axis, the acceleration becomes dependent on the azimuthal coordinate on the dipole surface φ (see Fig. 3). At a sufficiently small spin period and sufficiently large inclination of the magnetic dipole with respect to the disc plane, there are regions at the dipole surface where material can stay stably, i.e. the

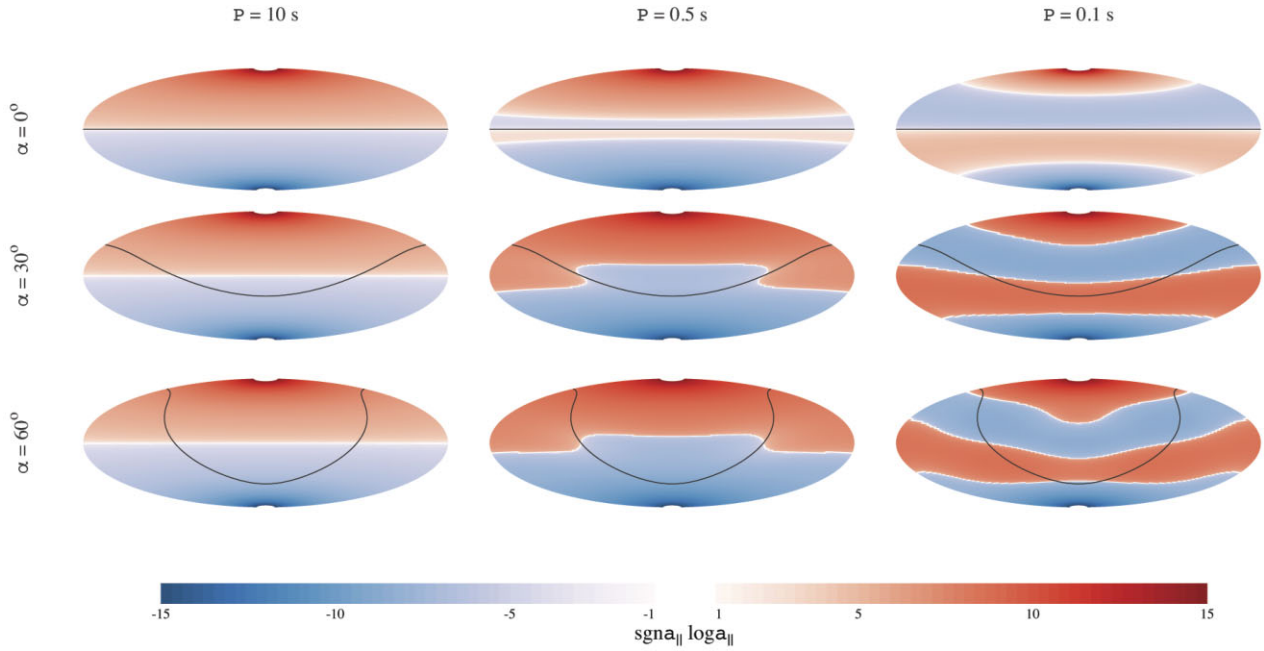

Figure 3. The colour maps represent acceleration along dipole magnetic field lines due to the gravitational and centrifugal forces at the magnetospheric surface. The red (blue) colour corresponds to the case of the acceleration directed towards the larger (smaller) latitudes, i.e. towards the upper (lower) pole of a star. The solid black line represents coordinates where the disc plane crosses the dipole surface. The magnetic obliquity is taken to be $\alpha = 0$ (the first line), 30° (the second line) and 60° (the third line). Left, middle, and right columns correspond to different NS spin periods: $P_{\rm spin} = 10$, 0.5, and 0.1 s, respectively. Parameters: $m = 1.4$, $R_{\rm m} = 10^8$ cm.

acceleration due to the gravitational and centrifugal forces is directed towards these regions (appearance of these regions was discussed by Abolmasov & Biryukov 2020 and Lyutikov 2023). The inclination of the magnetic dipole, initial accretion flow velocity, NS spin period, and thickness of the disc determine the regions where the material is collected.

Interaction of magnetospheric flow with X-ray photons emitted by the central objects results in appearance of radiative force. The radiative force is determined by local X-ray energy flux at the magnetospheric surface, the fraction of intercepted radiation and local inclination of magnetospheric surface in respect to the predominant direction of photons momentum. In the first approximation, the radiative force is directed in oppositely to the gravitational force. The fraction of intercepted X-ray photons is determined by the surface density of magnetospheric flow and mechanism of opacity. In our simulations, we assume that the opacity is dominated by the non-magnetic Compton scattering and taken to be $\kappa_{\rm e} = 0.34\,{\rm cm^2\,g^{-1}}$. Non-magnetic opacity is a valid approximation because magnetic field strength decreases rapidly with a distance from an NS and the cyclotron energy $E_{\rm cyc} \simeq 11.6\,B_{12}$ keV on the most of magnetospheric surface is much smaller then the typical energy of photons. In the limiting case of total absorption of radiation, the radiative force along the dipole field lines acting on a unit area can be estimated as

$$\frac{{\rm d}f_{\rm R}}{{\rm d}S}(\lambda) = \sin\chi\cos\chi\,\frac{F(\lambda)}{c}, \tag{15}$$

where $F(\lambda)$ is the photon energy flux. In the real situation, only a fraction of photons are absorbed/scattered by the envelope and contribute to be radiative force. Thus, equation (15) has to be rewritten as

$$\frac{{\rm d}f_{\rm R}}{{\rm d}S}(\lambda) = \sin\chi\cos\chi\,\frac{F(\lambda)}{c}\left(1-{\rm e}^{-\Sigma\kappa_{\rm e}/\sin\chi}\right), \tag{16}$$

where Σ is the local surface density of the magnetospheric flow. The estimation (16) assumes that the scattering is isotropic and, therefore, the photons effectively transfer their momentum to the accretion flow due to the first scattering event only. Equations (15) and (16) can be rewritten via the radiation force acceleration to keep the uniform with the previous description of the forces. The radiation acceleration inside the accretion flow is

$$a_{\rm rad}(\lambda) = \cos\chi\,\frac{\kappa_{\rm e}}{c}\,F(\lambda)\,{\rm e}^{-m\kappa_{\rm e}/\sin\chi}, \tag{17}$$

where m is Lagrangian coordinate of the point inside the flow. It is determined as ${\rm d}m = \rho\,{\rm d}z$, where z is a coordinate along the local normal to the magnetospheric surface, and ρ is the plasma mass density. The radiation acceleration averaged across the accretion flow is

$$a_{\rm rad}(\lambda,\,\Sigma) = \sin\chi\cos\chi\,\frac{F(\lambda)}{c\,\Sigma}\left(1-{\rm e}^{-\Sigma\kappa_{\rm e}/\sin\chi}\right), \tag{18}$$

where Σ is a total surface density integrated across the accretion flow at the given position. The last equation coincides with equation (16), if we take that $a_{\rm rad}(\lambda,\,\Sigma)\,\Sigma = {\rm d}f_{\rm R}/{\rm d}S$. In average, the photon scatterings following the first one do not affect the dynamics of the flow.

In the case of optically thick flow (i.e. $\Sigma\kappa_{\rm e} > 1$), the photon energy flux varies over the optical depth: some photons are scattered and reflected back by the surface layers, and only a fraction of photons penetrates deeper inside the flow covering magnetic dipole. Therefore, the acceleration due to the radiative force is dependent on the optical depth, and the layers located closer to the central source experience stronger accelerations. It might result in a gradient of velocity across the accretion channel. In this paper, we do not account for the influence of the radiative force gradient and possible effects of viscosity inside the accretion channel.

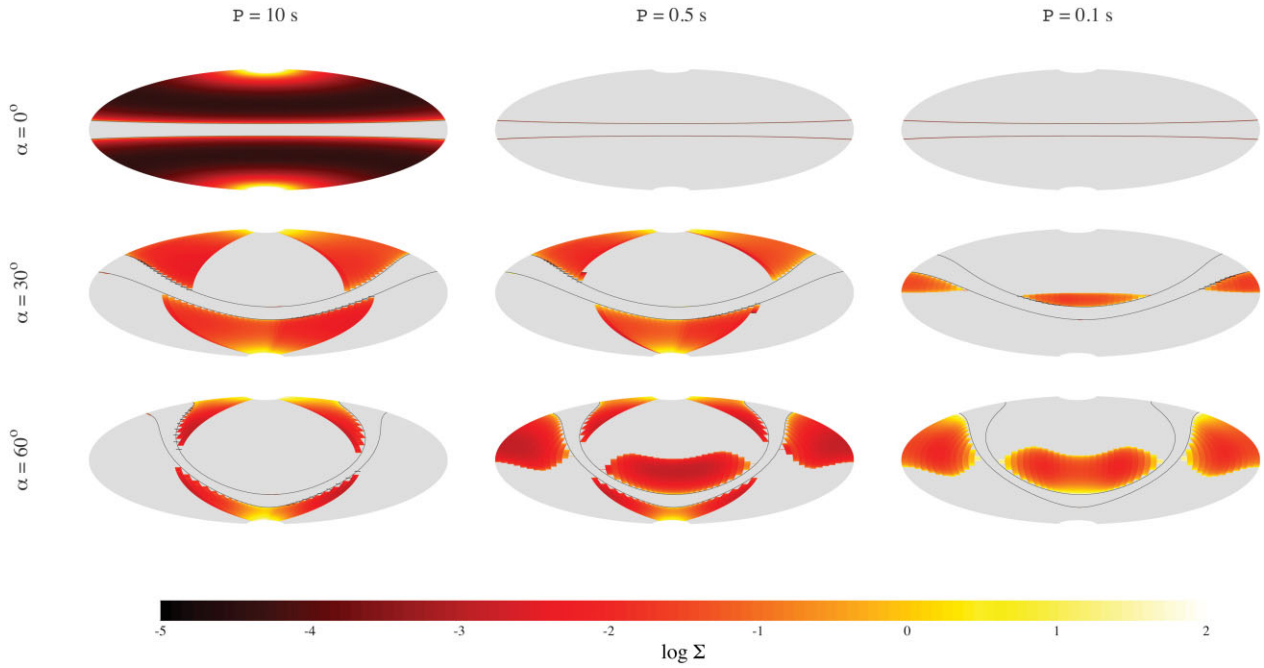

Figure 4. The maps illustrating the distribution of accretion flow surface density over the magnetospheric surface. Different maps correspond to different NS spin periods ($P = 10$, 0.5, and 0.1 s) and various magnetic obliquity α. The inclination of the magnetic axis with respect to the rotation axis of an NS results in a fractional covering of the magnetosphere. In panels corresponding to $\alpha = 0^\circ$ and $P = 0.5$ s, $\alpha = 0^\circ$ and $P = 0.1$ s, $\alpha = 30^\circ$ and $P = 0.1$ s, and $\alpha = 60^\circ$ and $P = 0.1$ s the accretion flow does not reach the NS surface due to the centrifugal force and we see the propeller effect in action. In the case of large obliquity, sufficiently fast rotation of an NS results in the appearance of regions where material tends to accumulate but does not move towards an NS. Parameters: $\dot{M}_{\rm m} = 10^{17}\,{\rm g\,s^{-1}}$, $m = 1.4$, $R_{\rm m} = 10^8$ cm.

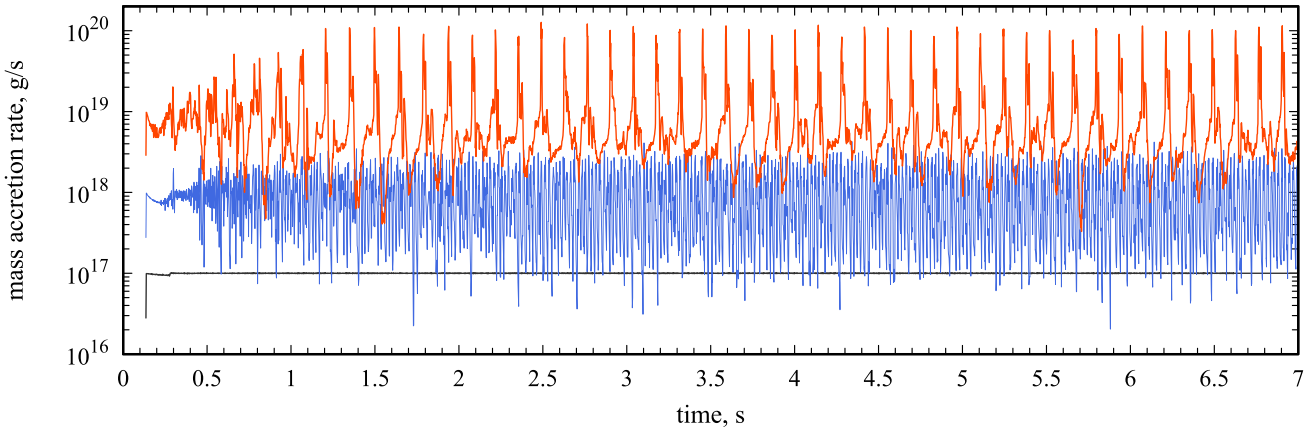

Figure 5. The mass accretion rate on to the NS surface calculated for different constant mass accretion rates at the inner disc radius: $\dot{M}(R_{\rm m}) = 10^{17}\,{\rm g\,s^{-1}}$ ($\sim 0.1\dot{M}_{\rm Edd}$, black line), $10^{18}\,{\rm g\,s^{-1}}$ ($\sim\dot{M}_{\rm Edd}$, blue line), and $10^{19}\,{\rm g\,s^{-1}}$ ($\sim 10\dot{M}_{\rm Edd}$, red line). In the case of low mass accretion rates (black line), the mass accretion rate at the NS surface replicates the mass accretion rate at the inner disc radius. Sufficiently high mass accretion rate from the disc results in appearance of instability of accretion process over the magnetospheric surface, which makes mass accretion rate at the NS surface strongly variable (blue and red lines). At the mass accretion rates $\sim 10^{19}\,{\rm g\,s^{-1}}$ from the disc (red line), the mass accretion rate at the stellar surface shows quasi-periodic oscillations. Parameters: $m = 1.4$, $R_{\rm m} = 10^8$ cm, $P_{\rm spin} = 10$ s, isotropic central source, and $\alpha = 0$.

2.3 Radiation from the neutron star surface

NS radius is expected to be much smaller than its magnetosphere (see equation 1), which is a good approximation in the case of XRPs. Thus, accounting for the influence of radiative force on the accretion flow dynamics, we consider an NS as a point source of X-ray radiation. Because accretion flow is directed towards NS magnetic poles by the stellar magnetic field, the emission from the central object can be strongly anisotropic. The angular distribution of X-ray luminosity is not known and described in our model by a special parameter $a_{\rm sp} \in [-1; +1]$ in our model:

$$\frac{{\rm d}L_i}{{\rm d}\Omega} \propto 1 + a_{\rm sp}|\cos\theta_{B,k}|, \tag{19}$$

where index $k \in \{1, 2\}$ denotes the pole of an NS, and $\theta_{B,i} \in [0, \pi]$ is the colatitude in the reference frame related to the magnetic dipole. Parameter $a_{\rm sp} = 0$ corresponds to the case of isotropic radiation from the central object, $a_{\rm sp} = -1$ corresponds to the fan beam diagram,

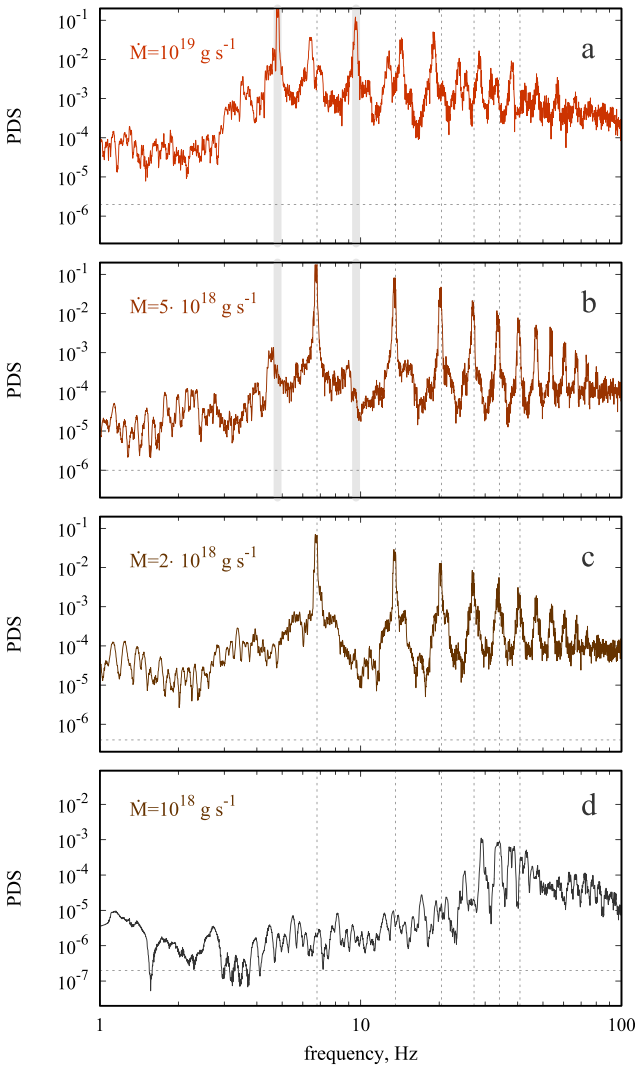

Figure 6. The modelled PDS of the mass accretion rate fluctuations at the NS surface. Different panels show the PDS for different mass accretion rates from the disc: 10^{19}, 5×10^{18}, 2×10^{18}, and 10^{18} g s^{-1} (from top to bottom). Parameters: $R_{\rm m} = 10^8$ cm, $P_{\rm spin} = 10$ s, isotropic source of emission.

and $a_{\rm sp} > 0$ corresponds to pencil beam diagram. The beam pattern is shaped by the geometry of the emitting region at the NS surface (Gnedin & Sunyaev 1973) and can be strongly influenced by the gravitational bending in the vicinity of an NS (Riffert & Meszaros 1988; Kraus 2001; Mushtukov et al. 2018).

The total luminosity of the central object $L_{\rm tot} = L_1 + L_2$ can be variable and dependent on the current mass accretion rate on to the poles of an NS. The mass accretion rate on one pole can be different from the mass accretion rate on another pole, which results in a difference between L_1 and L_2 and the corresponding X-ray energy flux at the magnetospheric surface:

$$F(\theta, t) = \frac{1}{r^2}\frac{{\rm d}L_{\rm tot}(t)}{{\rm d}\Omega}, \tag{20}$$

where r is determined by (4).

2.4 Mass accretion rate at the inner disc radius

The average mass accretion rate at the inner disc radius is a parameter of our simulations. It can be considered to be constant or variable due to fluctuating mass accretion rate in the disc (see e.g. Mushtukov et al. 2019b). Stochastic variability of the mass accretion rate at the inner disc radius is described by the power density spectra (PDS) and root-mean square (rms) variability. The broad-band component of the PDS in X-ray binaries is generally well described by a twice-broken power law (Hoshino & Takeshima 1993). In this paper, we restrict ourselves to investigating the effect of the rms on the magnetospheric accretion and, for simplicity, assume that the PDS is given by a power law in a given range of Fourier frequencies f, i.e.

$$\mathrm{PDS} \propto f^q, \tag{21}$$

where q is fixed at (-1). Because the disc can be geometrically thin or thick depending on the mass accretion rate (see estimations of the disc thickness in Suleimanov, Lipunova & Shakura 2007), the particles participating in our simulations start their motion along dipole magnetic field lines at $\lambda_0 \neq \lambda_{\rm d} = \pi/2 - \theta_{\rm d}$.

3 NUMERICAL MODEL

We consider a one-dimensional motion of accretion flow along dipole field lines given by (4). In the case of the rotational axis orthogonal to the disc plane (i.e. $\alpha = 0$), the accretion flow starts its motion at the latitude

$$\lambda_0 = \frac{\pi}{2} - \theta_{\rm d} \pm \delta\lambda, \tag{22}$$

where $\delta\lambda$ is determined by the semithickness of the accretion disc at the magnetospheric radius and reaches the NS surface at coordinate

$$\lambda_{\rm NS} \simeq \mathrm{acos}(\sqrt{R_{\rm NS}/R_{\rm m}}). \tag{23}$$

The accretion channel in between coordinates λ_0 and $\lambda_{\rm NS}$ is divided into N_λ intervals in λ-coordinate and N_φ intervals in the azimuthal angle. As a result, we construct a two-dimensional grid composed of $N_\lambda \times N_\varphi$ cells covering the magnetospheric surface. For the simulations represented in this paper, we have taken $N_\lambda = 630$ and $N_\varphi = 24$. Each simulation covers time interval of 30 s, is composed of a series of time-steps and traces the motion of quasi-particles along the field lines.

At each time-step of the simulation, we have information about the coordinates of all particles, their velocities and the total mass within each cell of a grid. At each time-step, we perform the following procedures:

(i) We start by determining the mass accretion rate at the inner disc radius based on the average mass accretion rate and rms of mass accretion rate variability. The mean mass accretion rate and its rms are parameters in our simulations. We follow the algorithm proposed by Timmer & Koenig (1995) to get a time series of the mass accretion rate and thus the mass accretion rate at a given moment. In our calculations, we take $q = -1$ and simulate the mass accretion rate time series on the base of assumed rms and PDS in the Fourier frequency interval $0.1\,\mathrm{Hz} < f < 100\,\mathrm{Hz}$. To model the time series, we take 5×10^3 frequencies in the considered frequency range (for details see Timmer & Koenig 1995).

(ii) We add $N_{\rm p}$ particles of equal mass to each of N_φ grid cells located near the edge of accretion disc, i.e. we add $N_{\rm p}N_\varphi$ particles. The mass of particles added to the grid at a given time-step t_i is related to the mass accretion rate $\dot{M}$ at the inner disc radius as

$$m_{{\rm p},j} = \frac{\dot{M}(t_i)\Delta t_i}{N_{\rm p}N_\varphi}, \tag{24}$$

where Δt_i is a time interval of the simulation and index j enumerates particles participating in a simulation. In the simulations represented

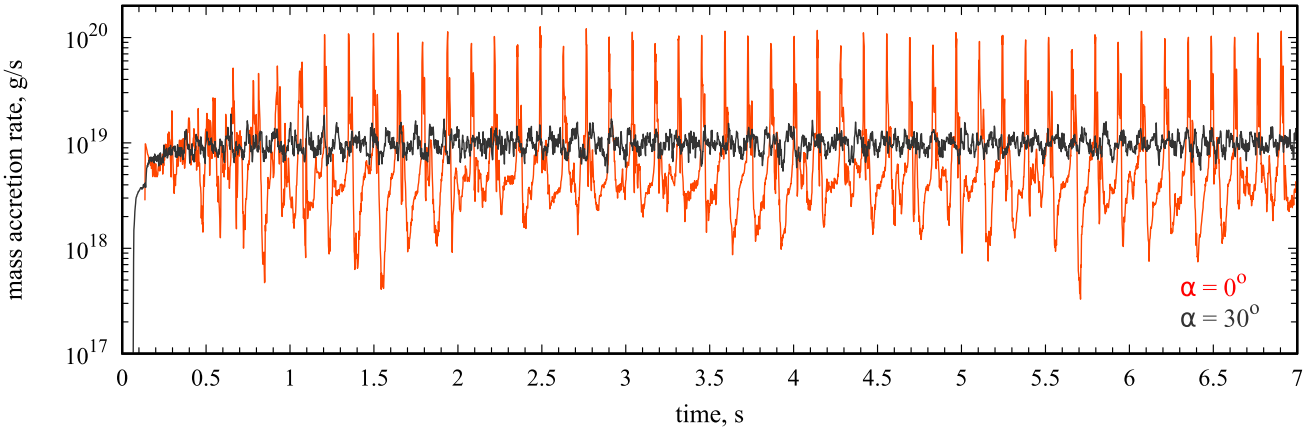

Figure 7. The mass accretion rate on to NS surface calculated for different inclinations of magnetic dipole in respect to the accretion disc plane: $\alpha = 0$ (red line) and $\alpha = 30^\circ$ (black line). The mass accretion rate at the inner disc radius is constant and fixed at $\dot{M} = 10^{19}\,\mathrm{g\,s^{-1}}$ ($\sim 10\dot{M}_{\rm Edd}$). Parameters: $m = 1.4$, $R_{\rm m} = 10^8$ cm, $P_{\rm spin} = 10$ s, isotropic central source.

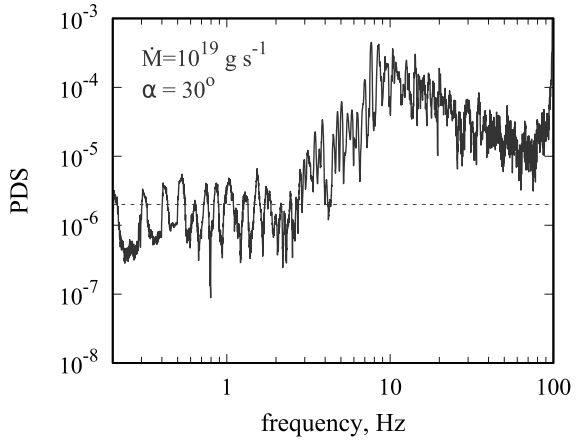

Figure 8. The modelled PDS of the mass accretion rate fluctuations on to the NS surface in a system, where an NS is inclined with respect to the disc plane. We do not see QPO peaks, but there is a broadband component appear at high frequencies ($\gtrsim$10 Hz). Horizontal dashed line illustrates the level of Poisson noise in the simulation. Parameters: $\dot{M} = 10^{19}\,\mathrm{g\,s^{-1}}$, $R_{\rm m} = 10^8$ cm.

in this paper, we use $N_\varphi = 24$ and $N_{\rm p} = 2$. The particles are injected to the accretion flow at a random position within the cell located at the accretion disc plane, i.e. the initial coordinates are

$$\lambda_j^{\rm (ini)} = \lambda_0 + X_j\,\frac{\lambda_{\rm NS} - \lambda_0}{N_\lambda}, \tag{25}$$

where $X_j \in (0;\,1)$ is a random number. The initial velocity of each particle along magnetic field lines $v_{\rm ini}$ is a parameter of the simulation. It is expected to be close to the thermal velocity of protons at the inner disc radius:

$$v_{\rm ini} \sim v_{\rm p} \approx 3\times 10^7\,T_{\rm keV}^{1/2}\,\mathrm{cm\,s^{-1}}, \tag{26}$$

where $T_{\rm keV}$ is the plasma temperature at $R_{\rm m}$ in units of keV. In our simulations we use $v_{\rm ini} \sim 10^7\,\mathrm{cm\,s^{-1}}$.

(iii) On the base of known coordinates of particles and their masses, we get the total mass in each cell of the grid and local surface density of the magnetospheric accretion flow $\Sigma(\lambda, \varphi, t_i)$.

(iv) We calculate the time interval towards the new time-step. The time-step of the simulation is variable and dependent on the typical particle velocities in the cells. It is taken to be sufficiently small to prevent particle transitions to the cells further than the nearest ones

$$\Delta t_i = \min\left\{\min_j\left[\frac{1}{5}\frac{(\mathrm{d}x/\mathrm{d}\lambda)\Delta\lambda_j}{v_j(t_i)}\right],\,10^{-5}\,\mathrm{s}\right\}, \tag{27}$$

where v_j is a velocity of a particle j, and the minimum is taken over all particles currently participating in simulation.

(v) We get the acceleration of particles along magnetic field lines. The particle motion is calculated by accounting for gravitational, radiation, and centrifugal forces (see Section 2.2). We calculate the vector sum of three forces for each cell of the grid and get acceleration along field lines for each particle currently participating in the simulation. The gravitational and centrifugal accelerations are not dependent on time and can be pre-calculated. The radiative force, on the contrary, can be variable due the variations of accretion luminosity and local surface density of accretion flow covering NS magnetosphere.

(vi) On the basis of calculated accelerations for particles, we get their velocities

$$v_j(t_{i+1}) = v_j(t_i) + a_j(t_i)\Delta t_i \tag{28}$$

and coordinates

$$\begin{aligned}
\lambda_j(t_{i+1}) &= \lambda_j(t_i) + \Delta\lambda_j(t_i),\\
\Delta\lambda_j(t_i) &= \frac{\Delta x_j(t_i)}{R_{\rm m}\cos\lambda_j(t_i)[1+3\sin^2\lambda_j(t_i)]^{1/2}},\\
\Delta x_j(t_i) &= \frac{v_j(t_{i+1}) + v_j(t_i)}{2}\Delta t_i.
\end{aligned} \tag{29}$$

(vii) We update the list of particles participating in the simulation. In particular, we account for particles accreted to the NS magnetic poles: particles that have reached one of the magnetic poles are taken into account when calculating the mass accretion rate and are removed from the list of particles. The mass accretion rate on to an NS magnetic pole is calculated as

$$\dot{M}_k(t_i) = \frac{\sum_j m_{{\rm p},j}^{(k)}}{\Delta t_i}, \tag{30}$$

where $k \in \{1,\,2\}$ denotes one of the magnetic poles and the summation is performed over the particles that have reached the surface in the time interval Δt_i. We also account for particles that have returned to the accretion disc. These particles remain in the simulation but are restarted from a random azimuthal coordinate at

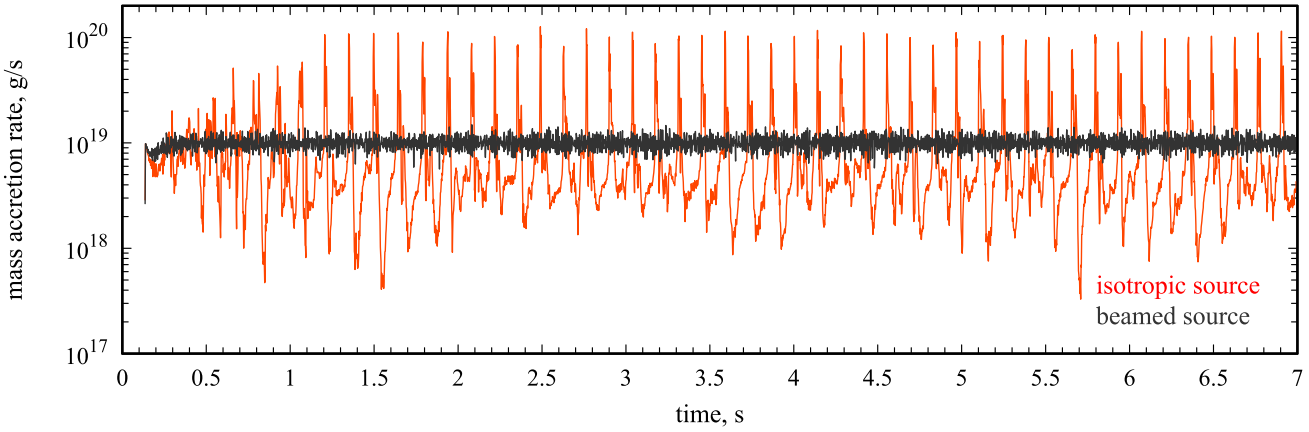

Figure 9. The mass accretion rate on to NS surface calculated for different beam patterns: the red line illustrates the case of isotropic central source, while the black line corresponds to the case of beamed emission from the poles of an NS (parameter $a_{\rm sp} = 2$ in equation 19). The mass accretion rate at the inner disc radius is constant and fixed at $\dot{M} = 10^{19}\,{\rm g\,s^{-1}}$. The rotation axis is taken to be orthogonal to the accretion disc plane. Parameters: $m = 1.4$, $R_{\rm m} = 10^8$ cm, and $P_{\rm spin} = 10$ s.

the next time-step. The mass accretion rate calculated in equation (30) and final velocity of particles are used to get accretion luminosity

$$L_k(t_i) = \frac{\sum_j (\gamma_j - 1) m^{(k)}_{{\rm p},j} c^2}{\Delta t_i}, \tag{31}$$

where $\gamma_j = [1 - (v_j/c)^2]^{-1/2}$ is the final Lorentz factor of a particle. The luminosity (31) is used to calculate photon energy flux (20) at the magnetospheric surface and then the radiative force at the next time-step of simulation.

(viii) We return to step (i).

Particle motion changes the mass density in each grid cell, and, as a result, the influence of three forces on the particles in the cells is recalculated at each time-step.

To investigate features of the mass accretion rate variability in the frequency domain, we redact the time series obtained by equation (30), where the time intervals between element of a time series are variable and short (see equation 27), which results in a Poisson noise. In particular, we combine nearby elements of the simulated time series into one and get an updated time series with larger and homogeneous time $\Delta t \simeq 2 \times 10^{-3}$ s. Using the updated time series of the mass accretion rate at the inner disc radius and at the NS surface, we calculate its Fourier transform:

$$\overline{\dot{M}}(f) = \Delta t \sum_{j=1}^{N_t} \dot{M}_k(t_j) {\rm e}^{2\pi i f t_j}, \tag{32}$$

where f is the Fourier frequency and N_t is a number of simulated points in the time series. The power density spectrum is calculated using normalization:

$${\rm PDS} = \frac{2}{M_{\rm acc}} \left| \overline{\dot{M}}(f) \right|^2 \tag{33}$$

where $M_{\rm acc} = \sum_{j=1}^{N_t} \dot{M}_k(t_j) \Delta t$ is the total mass accreted on to an NS during the time interval covered by a time series. Calculating the Fourier transform (32) and PDS (33), we exclude the first second of the simulation that is required for the accretion flow to reach the NS surface. The Nyquist frequency for the simulated time series is $f_{\rm N} = 0.5/\Delta t \simeq 250$ Hz and further we discuss PDS shape below this frequency only. In the case of normalization given by equation (33), the noise caused by finite number of particles participating in a simulation is expected at the level

$${\rm PDS}_{\rm noise} \approx \frac{2\,M_{\rm acc}}{N_{\rm tot}}, \tag{34}$$

where $N_{\rm tot}$ is a total number of particles accreted on to the stellar surface during the entire simulation.

To investigate stability of magnetospheric coverage by the accretion flow, we calculate the local average surface density, local averaged squared surface density

$$\begin{bmatrix} \langle \Sigma(\lambda,\varphi) \rangle \\ \langle \Sigma^2(\lambda,\varphi) \rangle \end{bmatrix} = \frac{1}{t_{\rm tot}} \sum_i \Delta t_i \begin{bmatrix} \Sigma(\lambda,\varphi,t_i) \\ \Sigma^2(\lambda,\varphi,t_i) \end{bmatrix}, \tag{35}$$

and its local standard deviation

$$\sigma_\Sigma(\lambda,\varphi) = \sqrt{\langle \Sigma^2(\lambda,\varphi) \rangle - \langle \Sigma(\lambda,\varphi) \rangle^2}. \tag{36}$$

4 RESULTS OF NUMERICAL SIMULATIONS

In our simulations of accretion flow dynamics, we initialize the flow at $t = 0$ from the edges of the accretion disc, which is fixed radius $R_{\rm m} = 10^8$ cm. It takes a fraction of a second (approximately 0.1 s for the specified $R_{\rm m}$) for the accretion flow to reach the NS surface. This duration is slightly longer than the free-fall time from the inner disc radius due to the flow following curved magnetic field lines. The radiative force comes into play as soon as the flow reaches the stellar surface. Before that, the flow dynamics is shaped by the gravitational and centrifugal forces only. In this section, we first discuss the results of simulations performed for a low mass accretion rates from the disc ($\dot{M} \lesssim 10^{17}\,{\rm g\,s^{-1}}$), when the influence of the radiative force can be neglected (Section 4.1). In the following we discuss the effects introduced by strong radiative force at high accretion rates ($\dot{M} \gtrsim \dot{M}_{\rm Edd} \sim 10^{18}\,{\rm g\,s^{-1}}$, Section 4.2).

4.1 The influence of gravitational and centrifugal forces

The accelerations along B-field lines due to the NS gravity and the centrifugal force are dependent on the mass of an NS, spin period, size, and inclination of the magnetic dipole with respect to the disc plane. The maps of this acceleration are pre-calculated (see Fig. 3). Sufficiently fast rotation of an NS magnetosphere results naturally in arising of the centrifugal barrier, i.e. the regions at the

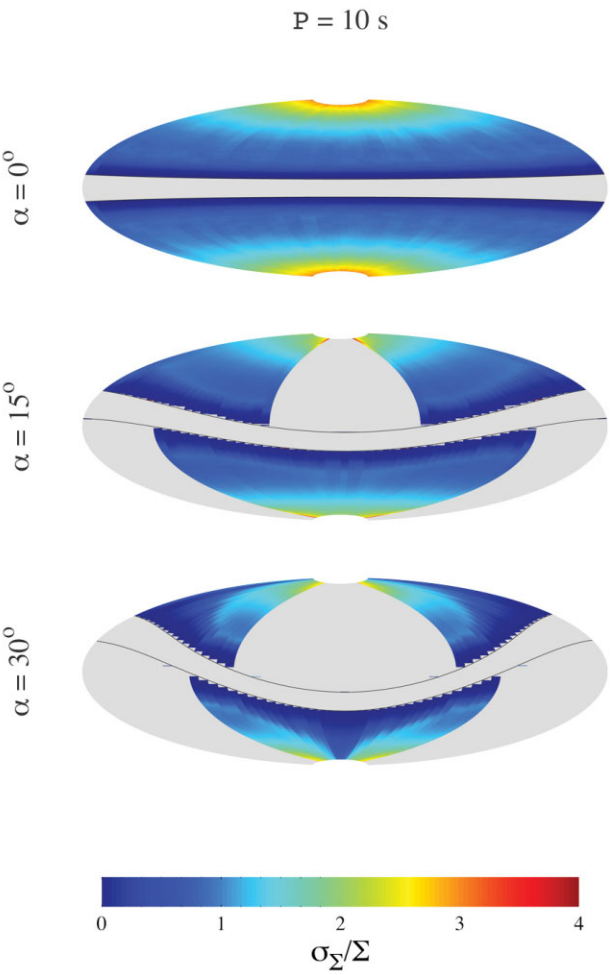

Figure 10. Maps of the relative standard deviation of the surface density (see equations 35 and 36) on the magnetospheric surface for the mass accretion rate fixed at $\dot{M}_{\rm m} = 10^{19}\,{\rm g\,s^{-1}}$ and different magnetic obliquity $\alpha = 0^\circ$, 15°, and 30° (from top to bottom). In the case of aligned rotation and magnetic axis, the relative variability of the surface density is stronger at larger latitudes. In the case of inclined magnetic dipole, only a fraction of magnetospheric surface is covered by accretion flow and the variability becomes dependent on the azimuthal angle: the regions located closer to the edges of accretion curtain tend to be more variable. Parameters: $m = 1.4$, $R_{\rm m} = 10^8$ cm, and $P = 10$ s.

magnetospheric surface, where the local acceleration is directed back to the disc plane. The centrifugal barrier is stronger in the case of faster rotation of an NS. It is expected that the material from the disc can penetrate through the centrifugal barrier in the case of the sufficiently high initial velocity of the material (in this case, the barrier slows down the flow but cannot stop it) or sufficiently large geometrical thickness of accretion disc, when the matter is collected from the upper layers of the disc (the latest effect was discussed by Çıkıntoğlu & Ekşi 2023).

In the case of an inclined magnetic dipole, there are regions at the inner disc radius where the centrifugal and gravitational forces prevent material motion towards one of the magnetic poles of an NS. It results in a partial covering of NS magnetosphere by the flow from the disc (see Fig. 4). Additionally, in the case of the sufficiently fast rotation of inclined magnetic dipole, there are regions at the NS magnetosphere where the projections of gravitational and centrifugal forces cancel each other. The appearance of these regions of stable equilibrium may result in local accumulation of accreting material (see Fig. 4). The fate of the matter locally accumulated at the magnetospheric surface might be affected by the cooling and heating processes. In particular, sufficiently fast cooling of matter accumulated at the magnetosphere can result in events of episodic accretion (Shakura et al. 2012). Analyses of heating and cooling processes, however, require specific analyses, which are out of the scope of this paper.

According to our simulations, the coverage of the NS magnetosphere is dependent both on the inclination of the magnetic dipole and NS spin period: the larger the inclination and the faster the rotation of an NS, the smaller the area of magnetosphere covered by accretion flow (see Fig. 4). We note that the arising of the 'propeller' effect in our simulations is dependent on the inclination of magnetic dipole: the spin period of 0.5 s is small enough to stop accretion in the case of $\alpha = 0^\circ$, but still allows accretion at $\alpha = 30^\circ$ and $\alpha = 60^\circ$ (see Fig. 4).

4.2 Radiative force coming into play

Influence of the radiative force depends on the mass accretion rate and corresponding energy release at the NS surface. At low, sub-Eddington ($\dot{M} \ll 10^{18}\,{\rm g\,s^{-1}}$), mass accretion rates, the radiative force does not play a significant role and stable mass accretion rate at the inner disc radius is replicated (with a time delay) at the stellar surface (see black line corresponding to $\dot{M} = 10^{17}\,{\rm g\,s^{-1}}$ in Fig. 5). High mass accretion rates, however, result in high luminosity and radiative force comparable to the gravitational and centrifugal forces. It causes instability of accretion flow at the mass accretion rates above the Eddington value ($\dot{M} \gtrsim 10^{18}\,{\rm g\,s^{-1}}$, see blue and red curves in Fig. 5 corresponding to the mass accretion rates $10^{18}\,{\rm g\,s^{-1}}$ and $10^{19}\,{\rm g\,s^{-1}}$ from the disc, respectively) and sharp increase in rms of the mass accretion rate variability at the NS surface. Sufficiently intensive mass inflow at the inner disc radius ($\dot{M} \gtrsim 10^{19}\,{\rm g\,s^{-1}}$) leads to quasi-periodic oscillations (QPOs) of the mass accretion rate at the stellar surface (see red line in Fig. 5). The time scale of the QPOs is close to the free-fall time-scale:

$$P_{\rm QPO} \approx \pi \left(\frac{R_{\rm m}^3}{2GM}\right)^{1/2} \simeq 0.2 \left(\frac{R_{\rm m,8}^3}{m}\right)^{1/2} \ {\rm s}. \tag{37}$$

The mechanism standing behind the QPOs is related to the influence of radiative force on the accretion flow and can be explained as follows: (i) accretion flow reaches NS surface and results in high luminosity of the central object; (ii) high luminosity leads to the radiative force, which is large enough to stop the flow on its way towards a star, (iii) mass accretion rate on to an NS drops as well as the accretion luminosity, which leads to a drop of the radiative force affecting the magnetospheric flow motion, (iv) under condition of small radiative force, accretion flow continues its motion towards an NS and reaches stellar surface within the free-fall time-scale, and (v) the cycle returns to the first step and continues quasi-periodically. The mass accretion rate on to one magnetic pole can differ from the mass accretion rate on to the other one. However, there is still a correlation between the two mass accretion rates.

In a high luminosity state, the PDS of the simulated time series of the mass accretion rate at the NS surface shows QPO peaks and its harmonics (see Figs 6a–c). In the range of mass accretion rate $2 \times 10^{18}\,{\rm g\,s^{-1}} \lesssim \dot{M} \lesssim 5 \times 10^{18}\,{\rm g\,s^{-1}}$, QPO appears at a frequency $\sim$7 Hz and is followed by a series of harmonics (see vertical dashed lines in Figs 6b and c). The frequency is almost independent on the mass accretion rate. The frequency of this QPO corresponds

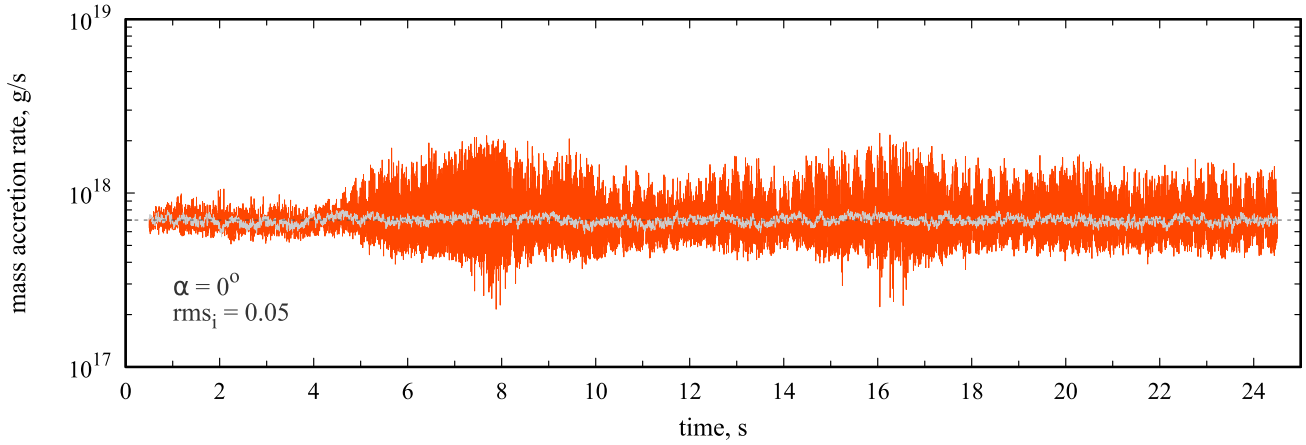

Figure 11. The mass accretion rate on to NS surface (red curve) calculated for the case of fluctuating mass accretion rate at the inner disc radius (grey curve). The average mass accretion rate at $R_{\rm m}$ is $\dot{M} = 7 \times 10^{17}\,{\rm g\,s^{-1}}$ (given by horizontal black dashed line), ${\rm rms}_i = 0.05$. One can see that fluctuations of the mass accretion rate at the NS surface are sensitive to the mass accretion rate at the inner disc radius. It is especially a case when the average mass accretion rate is close to the Eddington limit (as it is here). The rotation axis is taken to be orthogonal to the accretion disc plane. Parameters: $m = 1.4$, $R_{\rm m} = 10^8$ cm, $P_{\rm spin} = 10$ s, isotropic central source.

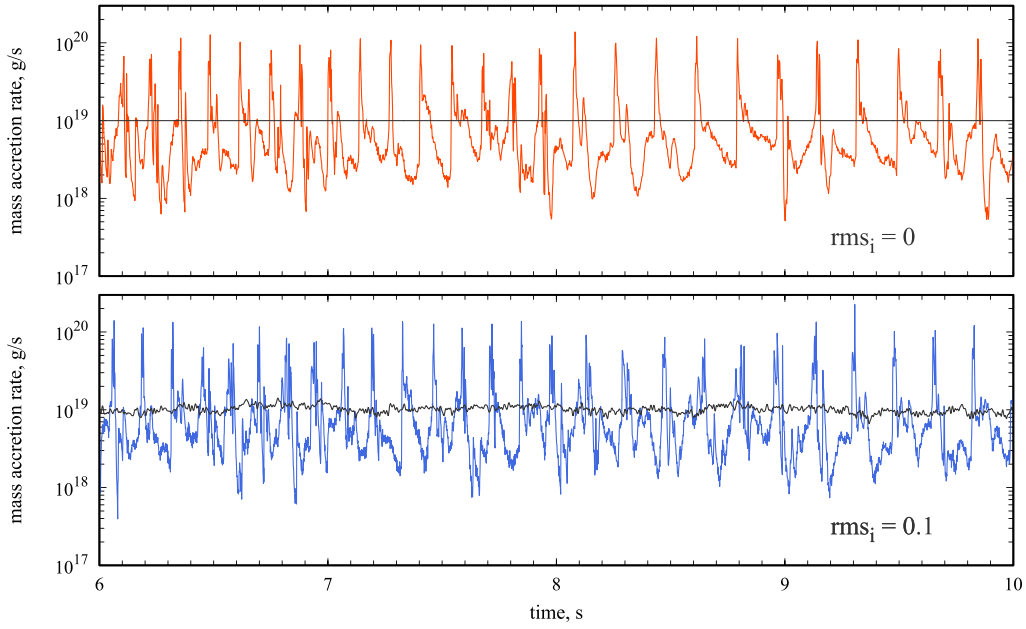

Figure 12. The red (blue) curve in the upper (lower) panel shows the mass accretion rate at the NS surface calculated for the case of constant (fluctuating) mass accretion rate at the inner disc radius. The latter is shown with a black line in the upper (lower) panel. The average mass accretion rate at $R_{\rm m}$ is $10^{19}\,{\rm g\,s^{-1}}$. In the lower panel, the rms of mass accretion rate fluctuations at $R_{\rm m}$ is taken to be 0.1. Parameters: $m = 1.4$, $R_{\rm m} = 10^8$ cm, $P_{\rm spin} = 10$ s, isotropic central source, and $\alpha = 0^\circ$.

to the time interval that is slightly shorter than the free-fall timescale (37). This discrepancy may be attributed to the non-zero initial velocity of the flow and the non-zero geometric thickness of the accretion disc. At mass accretion rates exceeding $\sim 5 \times 10^{18}\,{\rm g\,s^{-1}}$), we see a transition where the QPOs with a frequency of ∼7 Hz and its harmonics are gradually replaced by QPOs with a frequency of ∼5 Hz and its associated harmonics (see grey vertical shaded lines in Fig. 6a). This phenomenon is likely attributable to the diminishing radiative force, which decreases but does not entirely vanish, thereby continuing to influence the flow dynamics even during the intervals between quasi-periodic flares. The quality factors of the most distinct QPOs at high mass accretion rates reach a value of $\gtrsim$40. At relatively low mass accretion rate ($\sim 10^{18}\,{\rm g\,s^{-1}}$, see Fig. 6d), PDS of the mass accretion rate shows a broad hump at high frequencies ($\gtrsim$20 Hz).

The strength of QPOs of the mass accretion rate due to the influence of the radiative force is strongly affected by the inclination of NS magnetic dipole in respect to the accretion disc plane and beam pattern of X-ray radiation produces at the NS surface. Both inclination of magnetic dipole (see Fig. 7) and beaming of radiative pattern (see Fig. 9) stabilize the mass accretion rate at the stellar surface. In the case of accretion on to the inclined magnetic dipole, stabilization of accretion results in disappearance of QPOs from the PDS, but PDS shows broad-band high-frequency component (see Fig. 8).

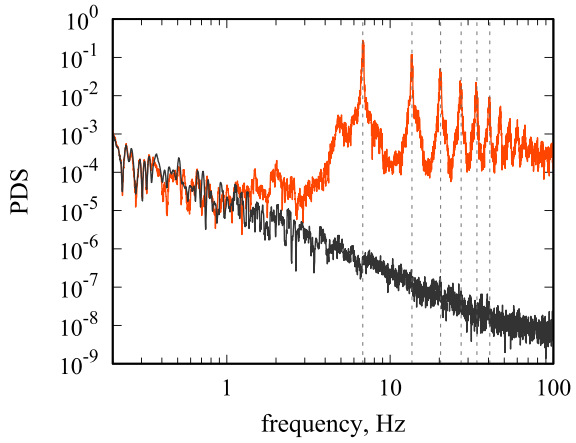

Figure 13. The modelled PDS of mass accretion rate fluctuations at the inner disc radius (black curve) and at the NS surface (red curve). One can see QPO at a frequency of ∼6.8 Hz and its five harmonics (their frequencies are shown by vertical dashed lines). Parameters: $\dot{M} = 10^{19}\,\mathrm{g\,s^{-1}}$ and $R_\mathrm{m} = 10^{8}$ cm.

Stabilization of accretion flow for the inclined magnetic dipole is attributed to the partial coverage of NS magnetosphere by the flow (see Fig. 4). Under this condition, a fraction of X-ray photons can freely leave a system without interaction with the magnetospheric flow. In addition, the flow covering NS magnetosphere has larger surface density Σ in comparison to the case of magnetic dipole aligned with accretion disc. The higher surface density results in a reduction of the average acceleration due to the radiative force, as described by equation (see equation 18).

Analysing the relative fluctuations in surface density across the magnetospheric surface [i.e. its local average value given by equation (35) and standard deviation given by equation (36)], it becomes evident that these fluctuations intensify towards the central object, as illustrated in Fig. 10. In the case of an inclined magnetic dipole, the strength of these fluctuations also exhibits azimuthal dependence. Specifically, surface density fluctuations are more pronounced towards the edges of the accretion curtain enveloping the magnetosphere, as highlighted in the lower panel of Fig. 10. It is essential to emphasize that these fluctuations in surface density hold the potential to significantly influence the process of pulse formation. A thorough exploration of this effect will be the focus of an upcoming publication.

Fluctuations of the mass accretion rate at the inner disc radius (caused by, in particular, the stochastic nature of viscous diffusion) do not affect qualitatively the process of magnetospheric accretion. The fluctuations at R_m increase rms of mass accretion rate variability at the NS surface. In the case of the average mass accretion rate close to the Eddington value, the fluctuating mass inflow at the magnetospheric boundary might result in variable rms of the mass accretion rate at the NS surface (see Fig. 11). It happens because the current mass accretion rate at R_m can be occasionally above the Eddington limit due to the fluctuations and then the magnetospheric accretion process turns into the unstable mode. At the mass accretion rates much larger than the Eddington limit (we have tested the average mass accretion rate $10^{19}\,\mathrm{g\,s^{-1}}$), the QPOs are preserved when fluctuations of the accretion rate at the inner disc radius are taken into account (see Figs 12and 13). A detailed analysis of accretion timing and calculation of mass accretion rate PDS requires, however, the simulation of long time series and will be discussed in a separate publication.

The initial velocity of the accretion flow at the inner disc radius (within the range $10^{6}\,\mathrm{cm\,s^{-1}} \lesssim v_\mathrm{ini} \lesssim 10^{7}\,\mathrm{cm\,s^{-1}}$) has only a negligible impact on the simulated time series of the mass accretion rate and its PDS. Note that the strength of the correlation between the mass accretion rate on to one and another magnetic pole can be dependent on the details of beam pattern formation and affected by light bending in the vicinity of an NS. We are planning to investigate these effects in a separate publication.

5 DISCUSSION AND SUMMARY

We conducted numerical simulations to explore the dynamics of accretion flow over the magnetosphere of bright XRPs. We assumed magnetic field geometry dominated by the dipole component and have taken into account the influence of the gravitational, centrifugal, and radiative forces. The magnetic dipole was taken to be inclined with respect to the plane of the accretion disc, while the rotation axis of an NS was assumed to be orthogonal to the disc, which is a good approximation for the case of accretion on to strongly magnetized NSs, where the surface field strength $B_0 \gtrsim 10^{11}$ G. These assumptions find support in the determination of geometrical parameters from several XRPs using polarimetric data from the Imaging X-ray Polarimetry Explorer (*IXPE*) observatory (see e.g. Doroshenko et al. 2022; Heyl et al. 2023; Malacaria et al. 2023; Mushtukov et al. 2023; Suleimanov et al. 2023; Tsygankov et al. 2023). The motion of accretion flow along the magnetospheric surface is constrained by the local direction of the magnetic field lines. Our calculations were performed under the assumption of opacity being dominated by non-magnetic Compton scattering. Deviations of the magnetic field geometry from the dipole one due to the accretion process (Lai 2014) can affect the dynamics of the magnetospheric accretion flow.[1] The calculation of magnetic field geometry perturbed by accretion requires the solution of the radiative magnetohydrodynamics (RMHD) equations, which is beyond the scope of this paper but will be done in the future publications.

Our examination of the accretion process under low mass accretion rates – where the influence of the radiative force is negligibly small – reaffirms findings previously reported in the literature: (i) For sufficiently small spin periods and inclined magnetic dipoles, specific regions on the magnetospheric surface exhibit material entrapment due to the interplay between gravitational and centrifugal forces (see Fig. 4; see also Abolmasov & Biryukov 2020; Lyutikov 2023). (ii) The conditions required for the occurrence of the 'propeller' effect are dependent on the geometrical thickness of accretion discs and inclination of a magnetic dipole with respect to the disc plane (Çıkıntoğlu & Ekşi 2023).

We have demonstrated that accretion flow over the NS magnetosphere is feasible but exhibits instability at super-Eddington mass accretion rates, particularly when the radiative force becomes influential in shaping the flow dynamics (see Fig. 5). This instability tends to be quasi-periodic, with a typical period closely aligning with the dynamical time-scale at the magnetospheric radius. Interestingly, the inclination of the magnetic dipole concerning the disc plane (see Fig. 7) and radiation beaming towards the axis of the magnetic dipole (see Fig. 9) act as stabilizing factors. Notably, quasi-periodic variability transforms into broad-band variability at high Fourier

[1]The degree of magnetic field distortion varies significantly depending on the model assumptions. In particular, the models proposed by Lipunov & Shakura (1980) and Aly (1980) predict relatively strong distortion, while the model by Lovelace, Romanova & Bisnovatyi-Kogan (1995) points to small field distortion within the magnetospheric radius.

frequencies (see Fig. 8). An unstable mass accretion rate on to the NS surface manifests as pronounced fluctuations in the surface density of matter covering the NS magnetosphere (see Fig. 10). Intriguingly, even under conditions of an inclined magnetic dipole and a relatively stable mass accretion rate on to the stellar surface, significant surface density fluctuations persist. These fluctuations atop a variable mass accretion rate at the NS surface can profoundly impact the pulse profile formation process, rendering pulsations unstable and challenging to detect. However, it is essential to note that this assumption requires validation through further numerical simulations.

Appearance of high-frequency QPOs and broad-band variability at high mass accretion rates was reported in bright X-ray transient GRO J1744−28, where the QPO frequency is $f_{\rm QPO} \simeq 40$ Hz (see e.g. Mönkkönen et al. 2019). If this QPO is associated with the instability of magnetospheric accretion flow, the inner disc radius is expected to be $\sim 2 \times 10^7$ cm. The appearance of high-frequency component ($f > 1$ Hz) of PDS at high mass accretion rates was reported in the other Galactic bright X-ray transient – *Swift* J0243.6+6124 (Doroshenko et al. 2020).

Possibly strong fluctuations of the mass accretion rate can affect the geometry of the emitting region in close proximity to an NS surface: the height of accretion columns (Basko & Sunyaev 1976; Lyubarskii & Syunyaev 1988; Mushtukov et al. 2015) is expected to be dependent on the mass accretion rate. Moreover, according to some theoretical models, variation of the mass accretion rate leads to fluctuating column height on the way to its stable state (Abolmasov & Lipunova 2023). Fluctuating geometry of the emitting region influences the beam pattern (Gnedin & Sunyaev 1973; Kraus 2001; Mushtukov et al. 2018) and formation of pulsation even without accounting for the influence of the magnetospheric accretion flow.

Detection of high-frequency QPOs can be difficult in the case of systems with strong radiation-driven outflows from the disc. The outflows should collimate X-ray photons from the central object. Due to the collimation process, the photons might experience a number of reflections/reprocessings by the walls of accretion cavity. As a result, one would expect suppression of any variability on time-scales smaller than the typical time-scale of photon travel inside the cavity (Mushtukov et al. 2021).

ACKNOWLEDGEMENTS

AAM thanks UKRI Stephen Hawking fellowship. AI acknowledges support from the Royal Society. VFS thanks Deutsche Forschungsgemeinschaft (DFG) grant WE 1312/59-1. The work was also supported by the German Academic Exchange Service (DAAD) travel grant 57525212 (VFS), the Academy of Finland grants 349144 and 349373, and the Väisälä Foundation (SST). We thank our anonymous referee for useful comments and suggestions that helped us improve the paper.

DATA AVAILABILITY

The calculations presented in this paper were performed using a private code developed and owned by the corresponding author; please contact him for any requests/questions about it. All the data appearing in the figures are available upon request.

REFERENCES

Abolmasov P., Biryukov A., 2020, MNRAS, 496, 13
Abolmasov P., Lipunova G., 2023, MNRAS, 524, 4148
Aly J. J., 1980, A&A, 86, 192
Arons J., Lea S. M., 1976, ApJ, 207, 914
Bachetti M. et al., 2014, Nature, 514, 202
Basko M. M., Sunyaev R. A., 1976, MNRAS, 175, 395
Burnard D. J., Arons J., Lea S. M., 1983, ApJ, 266, 175
Carpano S., Haberl F., Maitra C., Vasilopoulos G., 2018, MNRAS, 476, L45
Chashkina A., Lipunova G., Abolmasov P., Poutanen J., 2019, A&A, 626, A18
Çıkıntoğlu S., Ekşi K. Y., 2023, MNRAS, 524, 1727
Doroshenko V. et al., 2020, MNRAS, 491, 1857
Doroshenko V. et al., 2022, Nat. Astron., 6, 1433
Fabrika S. N., Atapin K. E., Vinokurov A. S., Sholukhova O. N., 2021, Astrophys. Bull., 76, 6
Frank J., King A., Raine D. J., 2002, Accretion Power in Astrophysics, 3rd edn, Cambridge University Press, Cambridge
Fürst F. et al., 2016, ApJ, 831, L14
Gnedin Y. N., Sunyaev R. A., 1973, A&A, 25, 233
Heyl J. et al., 2023, preprint (arXiv:2311.03667)
Hoshino M., Takeshima T., 1993, ApJ, 411, L79
Illarionov A. F., Sunyaev R. A., 1975, A&A, 39, 185
Israel G. L. et al., 2017a, Science, 355, 817
Israel G. L. et al., 2017b, MNRAS, 466, L48
Jiang Y.-F., Stone J. M., Davis S. W., 2014, ApJ, 796, 106
King A. R., 2009, MNRAS, 393, L41
King A., Lasota J.-P., 2020, MNRAS, 494, 3611
King A., Lasota J.-P., Kluźniak W., 2017, MNRAS, 468, L59
King A., Lasota J.-P., Middleton M., 2023, New Astron. Rev., 96, 101672
Kraus U., 2001, ApJ, 563, 289
Kulkarni A. K., Romanova M. M., 2008, MNRAS, 386, 673
Lai D., 2014, in EPJ Web Conf., 01001
Lipunov V. M., Shakura N. I., 1980, Sov. Astron. Lett., 6, 14
Lovelace R. V. E., Romanova M. M., Bisnovatyi-Kogan G. S., 1995, MNRAS, 275, 244
Lyubarskii Y. E., Syunyaev R. A., 1988, Sov. Astron. Lett., 14, 390
Lyutikov M., 2023, MNRAS, 520, 4315
Malacaria C. et al., 2023, A&A, 675, A29
Markozov I. D., Mushtukov A. A., 2024, MNRAS, 527, 5374
Mönkkönen J., Tsygankov S. S., Mushtukov A. A., Doroshenko V., Suleimanov V. F., Poutanen J., 2019, A&A, 626, A106
Mönkkönen J., Tsygankov S. S., Mushtukov A. A., Doroshenko V., Suleimanov V. F., Poutanen J., 2022, MNRAS, 515, 571
Mushtukov A. A., Portegies Zwart S., 2023, MNRAS, 518, 5457
Mushtukov A., Tsygankov S., 2022, preprint (arXiv:2204.14185)
Mushtukov A. A., Suleimanov V. F., Tsygankov S. S., Poutanen J., 2015, MNRAS, 447, 1847
Mushtukov A. A., Suleimanov V. F., Tsygankov S. S., Ingram A., 2017, MNRAS, 467, 1202
Mushtukov A. A., Verhagen P. A., Tsygankov S. S., van der Klis M., Lutovinov A. A., Larchenkova T. I., 2018, MNRAS, 474, 5425
Mushtukov A. A., Ingram A., Middleton M., Nagirner D. I., van der Klis M., 2019a, MNRAS, 484, 687
Mushtukov A. A., Lipunova G. V., Ingram A., Tsygankov S. S., Mönkkönen J., van der Klis M., 2019b, MNRAS, 486, 4061
Mushtukov A. A., Portegies Zwart S., Tsygankov S. S., Nagirner D. I., Poutanen J., 2021, MNRAS, 501, 2424
Mushtukov A. A. et al., 2023, MNRAS, 524, 2004
Nelson R. W., Wang J. C. L., Salpeter E. E., Wasserman I., 1995, ApJ, 438, L99
Poutanen J., Lipunova G., Fabrika S., Butkevich A. G., Abolmasov P., 2007, MNRAS, 377, 1187
Raguzova N. V., Lipunov V. M., 1998, A&A, 340, 85
Reig P., 2011, Ap&SS, 332, 1
Riffert H., Meszaros P., 1988, ApJ, 325, 207
Shakura N. I., Sunyaev R. A., 1973, A&A, 24, 337
Shakura N., Postnov K., Kochetkova A., Hjalmarsdotter L., 2012, MNRAS, 420, 216
Staubert R. et al., 2019, A&A, 622, A61

Suleimanov V. F., Lipunova G. V., Shakura N. I., 2007, Astron. Rep., 51, 549
Suleimanov V. F. et al., 2023, A&A, 678, A119
Timmer J., Koenig M., 1995, A&A, 300, 707
Tsygankov S. S., Doroshenko V., Lutovinov A. A., Mushtukov A. A., Poutanen J., 2017, A&A, 605, A39
Tsygankov S. S. et al., 2023, A&A, 675, A48
Ustyugova G. V., Koldoba A. V., Romanova M. M., Lovelace R. V. E., 2006, ApJ, 646, 304
Wang Y. M., Frank J., 1981, A&A, 93, 255
Zel'dovich Y. B., Shakura N. I., 1969, SvA, 13, 175
Zhang L., Blaes O., Jiang Y.-F., 2022, MNRAS, 515, 4371

This paper has been typeset from a TEX/LATEX file prepared by the author.